MNRAS 000, 000–000 (0000) Preprint 4th April 2018 Compiled using MNRAS LATEX style file v3.0

Companion accretion in common envelope evolution

Luke Chamandy[1]⋆, Adam Frank[1]†, Eric G. Blackman[1]‡, Jonathan Carroll-Nellenback[1], Baowei Liu[1], Zhuo Chen[1], Jason Nordhaus[2,3], Yisheng Tu[1]and Bo Peng[1] (tentative)
[1]*Department of Physics and Astronomy, University of Rochester, Rochester NY 14618, USA*
[2]*National Technical Institute for the Deaf, Rochester Institute of Technology, NY 14623, USA*
[3]*Center for Computational Relativity and Gravitation, Rochester Institute of Technology, NY 14623, USA*

4th April 2018

ABSTRACT
[Eric: Binaries are likely needed to explain the ubiquity of bipolar planetary nebulae (PNe) and pre-planetary nebulae (pPNe). The binary central stars of several bipolar PNe are close enough to imply that they, and likely many more, experienced common envelope (CE) interaction, whereby the core of the original asymptotic giant branch (AGB) star and its companion rapidly spiralled in toward [Luke: one] another, and ejected the envelope. CE evolution [Luke: (CEE)] is presently poorly understood and is computationally demanding. Simulations have yet to conclusively determine how the envelope is ejected and a tight binary results if only the binary potential energy is used to propel the envelope. Additional power sources might be necessary. Accretion onto the in-spiraling companion is one such source. Accretion is likely common in post-AGB binary interactions but how it operates and how its consequences depend on binary separation remain open questions. Here we use high resolution global 3-D hydrodynamic simulations of CEE with the AMR code AstroBEAR, to bracket the range of CEE companion accretion rates by comparing runs that remove mass and pressure via a subgrid accretion model with those that do not. The results show that if a pressure release valve is available, super-Eddington accretion may be common. Jets are a plausible release valve in these environments, and they could also help unbind and shape the envelopes.]

Key words: binaries: close – accretion, accretion discs – stars: kinematics and dynamics – hydrodynamics – methods: numerical

1 INTRODUCTION

2 METHODS

2.1 Setup

Simulations are performed with the adaptive mesh refinement (AMR) multiphysics code AstroBEAR (Cunningham et al. 2009; Carroll-Nellenback et al. 2013). Our numerical setup and chosen physical parameter values follow closely those of Ohlmann et al. (2016, 2017) (hereafter ORPS16 and ORPS17, respectively), although the numerical methods are very different from theirs (e.g. AMR vs. moving mesh). In particular, the setup and preparation of the red giant (RG) star is very similar to theirs with a few minor differences discussed below, and was chosen to be such for two reasons. First, the method had been shown to result in a star with remarkably small deviations from hydrostatic equilibrium. Second, this choice enables a consistency check between independently obtained results, namely ours and theirs.

Below we summarize the procedure. The reader is referred to ORPS17 for details, and we remark on any important differences between the two approaches below. We first evolve a star with a zero-age main sequence mass of $2M_\odot$ using the 1D stellar evolution code MESA (version 8845) (Paxton et al. 2011, 2013, 2015), setting the metallicity Z to 0.02, and select the snapshot that most closely coincides with the RG of ORPS16; ORPS17 on the Hertzsprung-Russell diagram. This star we refer to below as the primary, while we refer to its companion as the secondary.

Resolving the pressure scaleheight in the core is not numerically feasible. This is addressed by truncating the RG at a radius $r = r_\mathrm{c} = 2.41R_\odot$, and replacing the core with the combination of a gravitation-only sink particle and a modified profile which matches smoothly the density at r_c. The modified profile is obtained by solving numerically a modified Lane-Emden equation, with polytropic index $n = 3$, that takes into account the gravitation of the sink particle, and also satisfies the boundary conditions for ρ and $d\rho/dr$. Below we sometimes refer to this particle as the primary particle and to the remainder of the RG as the primary envelope, and [Luke: to] their masses by M_1 (primary), m_1 (primary particle) and $m_{1,\mathrm{env}}$ (primary envelope). Unlike in ORPS16; ORPS17, where the sink particle mass m_1 is set equal to the interior mass $m(r_\mathrm{c})$ of the MESA profile, we iterate over m_1, solving the equation at each iteration until $m_1 + m_{1,\mathrm{env}}(r_\mathrm{c}) = m(r_\mathrm{c})$, where $m(r)$ is the interior

⋆ lchamandy@pas.rochester.edu
† afrank@pas.rochester.edu
‡ blackman@pas.rochester.edu

mass and $m_{1,\mathrm{env}}(r_c)$ is the interior gas mass of the modified profile. This prevents the mass of the modified RG exceeding slightly that of the original MESA RG, and more importantly, it allows one to maintain a higher degree of hydrostatic equilibrium in the RG. The initial mass and radius of the primary are $M_1 = 1.956 M_\odot$ and $R_1 = 48.1 R_\odot$, respectively, with the sink particle at the RG centre having mass $m_1 = 0.369 M_\odot$.

[Eric: a little confusing as reader think centre would be fixed in centre of mass frame] [Luke: Simulations are] carried out in the inertial centre of mass frame, but with [Luke: the centre of the mesh coinciding with the initial position of the primary particle.] [Luke comments: The centre of the mesh is fixed in the inertial frame, it does not move around with the primary particle. Not sure if this was the confusion. In any case hopefully the meaning is clear now?] We choose extrapolating hydrostatic boundary conditions and adopt a multipole expansion method for solving the Poisson equation. The ambient medium is chosen to have constant density and pressure of $6.67 \times 10^{-9}\,\mathrm{g\,cm^{-3}}$ and $1.01 \times 10^{5}\,\mathrm{dyn\,cm^{-2}}$; these values are similar to the values at the surface of the RG. The ambient pressure (some seven orders of magnitude smaller than the central pressure of the modified envelope) is added everywhere in the domain to obtain a smooth transition between the stellar surface and its surroundings. It is chosen just large enough to ensure that the pressure scaleheight is adequately resolved at the stellar surface. Using a lower ambient density results in larger ambient sound speeds and smaller timesteps, resulting in reduced computation speed. In lower resolution tests we found that reducing the ambient density to $10^{-10}\,\mathrm{g\,cm^{-3}}$ makes no significant difference in the region of interest. We also experimented with invoking a hydrostatic atmosphere instead of a uniform ambient medium, but found that this results in numerical instabilities arising at the corners of the mesh.

A second sink particle with mass equal to half that of the RG, or $m_2 = 0.978 M_\odot$, is placed at a distance $a_0 = 49.0 R_\odot$ from the primary sink particle, just outside of the RG, at $t = 0$. This particle represents either a main sequence star or a white dwarf. For both particles, a spline function (Springel 2010) is used with softening length r_s set to be equal to r_c. The particles and RG envelope are initialized in a circular Keperian orbit. Unlike RT08; RT12; ORPS16, the RG envelope is not initialized to have a spin relative to the centre of mass reference frame. [Luke comments: Make argument based on Macleod's new simulations that if RG was spinning in corotation with orbit at the start of Roche lobe overflow, it would no longer be spinning at this rate. So it is not fully clear what value to use. In future we hope to try simulating different spins. It would also be interesting to try different initial separations, but for now we are limited by computational resources.]

Below we compare two runs, which we refer to as Model A and Model B. The main difference is that a sub-grid accretion model is implemented only for Model B. However, the setups for these runs are otherwise slightly different. Model A uses a box with side length $L = 1150 R_\odot$, while for Model B $L = 575 R_\odot$. For Model B, we apply the velocity damping algorithm of ORPS17 until $5 t_\mathrm{dyn}$, with t_dyn set to 3.5 d, but for Model A we do not apply any velocity damping. We performed low resolution tests with and without damping, and found that it made very little difference to the particle orbital evolution and CE morphology. Further, we studied plots of gas density, pressure and sound speed between $t = 0$ and $t = 1.2$ d to measure the differences between the two simulations. [Luke comments: Yisheng is still improving this analysis which will result in one or two sentences to quantify the difference, and some plots that could go into an appendix if say the referee complains, but so far the difference between the two runs looks to be acceptably small.]

The highest spatial resolution of $0.140 R_\odot$ and base resolution of the ambient volume of $2.25 R_\odot$ are both the same for Models A and B, and there is a buffer zone in between to allow the resolution to transition gradually. The region within which maximum refinement is performed by the code is slightly different in extent and shape for Models A and B, as are the extents of the buffer zones.[1] For both runs, however, the region of maximum refinement moves along with the particles and contains them (as well as a portion of the surrounding gas) at all times, so that the resolution is both uniform and very high in the region of interest. In addition, the softening length for the sink particles is reduced to half of its initial value about halfway through the simulation for Model A, while the smallest resolution cell was halved to $0.070 R_\odot$, but not for Model B. This step was taken to ensure that the softening length never exceeded the somewhat arbitrary fraction of 1/5 of the inter-particle separation (cf. ORPS16). Limited computational resources prohibit us from redoing one of the runs to make these parameter values match more precisely, but we are confident that these differences result in only minor differences in the results and do not affect our conclusions. Finally, Model A was run up to 40 d, while Model B was run up to 69 d but we choose to present results for the first 40 d only.

2.2 Modelling the accretion

Model A does not employ a sub-grid accretion model, and thus resembles closely the setup of ORPS16, and, to a lesser extent those of the other global CE simulations from the literature which also do not have sub-grid accretion. On the other hand, Model B employs the accretion model of Krumholz et al. (2004) for the secondary, but not for the primary particle[Luke: , because our goal is to explore accretion onto the secondary.][2] This prescription is based on the Bondi-Hoyle-Lyttleton formalism (Hoyle & Lyttleton 1939; Bondi & Hoyle 1944; Bondi 1952, see Edgar 2004 for a review).

It has been argued that the Bondi-Hoyle-Lyttleton formalism overstimates the accretion rate in CE evolution (Ricker & Taam 2008, 2012; MacLeod & Ramirez-Ruiz 2015; MacLeod et al. 2017). It is not our intention here to argue this point one way or the other. Rather we wish to explore what happens when we allow the secondary to accrete at a high but still plausible rate, and the Krumholz et al. (2004) model, being well-motivated physically and well-tested numerically [Luke: (Li et al. 2014)], is currently the best tool we have for this purpose.

Accretion is permitted to take place within a zone of four grid cells from the secondary. Krumholz et al. (2004) suggests that the *Plummer* softening radius should be smaller or equal to the accretion radius, to avoid artificially reducing the accretion rate due to the reduced gravitational acceleration inside the softening sphere. The spline potential employed is roughly equivalent to a Plummer potential with a Plummer softening radius that is 2.8 times smaller than the spline softening radius of ≈ 17 grid cells (this factor gives equal values of the potential at the origin). Thus, the accretion radius (4 cells) is close to but slightly smaller than the Plummer-equivalent softening radius (≈ 6 cells), which implies that the accretion rate

[1] For Model A, this region is spherical and centred on the primary particle until $t = 16.7$ d, after which it is centred on the secondary. For Model B, there are two such overlapping regions, one spherical centred on the primary particle, and the other cylindrical with axis [Luke: orthogonal to the orbital plane] and centred on the secondary.

[2] [Luke: In any case, we shall see in Section 3.2 that while the flow around the secondary has certain properties expected for an accretion flow even in Model A (no sub-grid accretion), the same cannot be said about the flow around the primary particle.]

is likely to be reduced somewhat from the value it would have had had the two radii been set equal. In this sense, the sub-grid model employed can be thought of as a slightly "milder" version of Krumholz et al. (2004).

3 RESULTS

3.1 Description of runs

In Figures 1 and 2 we present snapshots of slices of gas density in the orbital plane at $t = 0$, 10, 20 and 40 d, for Models A and B, respectively, with axes in units of $R_\odot$, and density in units of $\mathrm{g\,cm^{-3}}$. These figures and others to follow are drawn such that the secondary is located at the centre and the primary point particle is to its left, with the spline softening sphere depicted with a green circle around each particle. These snapshots can be thought of as frames from a movie taken in a reference frame rotating with the instantaneous angular velocity of the particles. The global evolution is very similar between the two runs, and closely agrees, at least qualitatively, with the results of ORPS16. The spiral shock morphology that develops is also consistent with the results of other global CE simulations more generally.

The distance between the two particles in the orbital plane a as a function of time is illustrated in Figure 3, solid blue for Model A and dashed light blue for Model B. Jagged solid red and dashed orange lines are plotted to show the radius of the sphere within which the resolution is at the highest refinement level, while solid green and dashed light green show the spline softening radius, for Models A and B respectively. The initial reduction in separation for the first ~ 12 d is known as the plunge-in phase, and each subsequent oscillation corresponds to a full orbit of 2π radians.

The curves for Models A and B are almost identical up to about $t = 15$ d, at which point they begin to diverge slightly. This time does not correspond to any change in refinement radius or softening length, but it does correspond approximately to the peak of the accretion rate for Model B, as will be discussed in Section 3.2. Therefore, the initial difference at least can be safely concluded to be caused by the difference in accretion prescriptions between the two runs. In Model A, 10 orbits are completed by $t = 40$ d, while in Model B, 9 orbits are completed, so the mean orbital frequency is higher in Model A between $t = 15$ d and $t = 40$ d than for Model B. This is consistent with the mean inter-particle separation being slightly lower for Model A than for Model B during the same time interval. However, a closer look tells us that from $t \sim 15$–17 d, Model B shows a smaller separation and mean orbital period than Model A, while Model B shows a larger separation and mean orbital period than Model A after $t \sim 17$ d. This suggests that the reduction in softenening length causes the orbital period to decrease in Model A after $t \sim 17$ d, compared to what it would have been had the softening length remained the same. However, between $t \sim 15$–17 d, the sub-grid accretion causes the orbital period to reduce in Model B from what it would have been had sub-grid accretion been turned off. Therefore, both sub-grid accretion and reduction of the softening length tend to reduce the orbital period and mean separation. We elaborate on this point in Sections 3.2 and 4.

Both curves of separation vs. time resemble qualitatively that of ORPS16. However, in that work the particles complete only 7 orbits by $t = 40$ d. Moreover, the first minimum is lower than the second, which is not the case in our runs, where the minima and maxima decrease monotonically with time. The main cause for these differences is probably the fact that in ORPS16 the RG is initialized with a solid body rotation of 95% corotation, whereas in our case the initial angular rotation speed is zero, but it would be interesting to explore the effects of initial spin in a future study.

We now turn to the insets of Figure 3, where the orbits are plotted for Model A on the left and for Model B on the right. The orbit of the primary particle is shown in blue shades and the secondary in red/orange shades.[3] The spline softening spheres are indicated with green circles for $t = 0$ and, for Model A, also for $t = 16.7$ d, when the softening length is halved. Orbits resemble qualitatively the orbit obtained by ORPS16.

Next we show, in Figure 4, slices of ρ at $t = 40$ d that pass through both particles and which cut through the orbital plane orthoganally, so that the view is edge-on with respect to the particles' orbit. The left-hand column shows results for Model A while the right-hand column shows results for Model B, and the top and bottom rows present different levels of zoom. The layered shock morphology is qualitatively very similar to that seen in other CE simulations (e.g. Iaconi et al. 2017). Models A and B also show quite similar morphology but with one conspicuous difference. A torus-shaped structure is present around the secondary in Model B, which employs sub-grid accretion, but is absent in Model A. This structure is reminiscent of a thick accretion disc [Luke comments: make reference to ADAF here?] and is accompanied by a low-density elongated bi-polar structure, seen in blue in the bottom-right panel of Figure 4. Clearly, accretion is the cause for the presence of this striking morphology in Model B. Below we examine the properties of the flow around the companion in more detail for both runs.

3.2 Accretion

We have established that accretion affects both the orbit of the particles and the morphology of gas around the secondary. We now explore the flow of gas toward and away from the secondary in more detail.

3.2.1 'Accretion' in the absence of a sub-grid model

For Model A, sub-grid accretion is turned off, but we can measure the rate of mass flowing toward the secondary. We do this by following RT08; RT12 in plotting the gas mass inside spheres of a given radius centred on the secondary against time in the top panel of Figure 5. The blue curves and left-hand vertical axis represent the accumulated gas mass $\Delta M_{\mathrm{in},2}$, while the red curves and right-hand vertical axis show the accretion rate $\dot{M}_{\mathrm{in},2}$, for each of the control spheres whose radius appears in the legend. These quantities are obtained by integrating the gas mass inside the control sphere at each time and then differentiating the resulting time series to obtain a rate. The green vertical line indicates the time at which the softening length is halved. For reference, we remind the reader that the mass of the secondary sink particle is $m_2 = 0.978 M_\odot$, and that of the primary sink particle is $m_1 = 0.369 M_\odot$.

The qualitative behaviour is approximately independent of the control radius, or put another way, the curves differ in amplitude but are very similar in shape. This tells us that the flow near the secondary is 'global,' in the sense that the gas at different radii moves inward or outward at the same time (on average over each spherical surface). We see that the inflow rate is relatively small until $t \approx 10$ d, and that it peaks shortly thereafter, between $t \approx 12.5$ d

[3] [Luke: The sampling rate used to draw the orbits in Figure 3 is about one frame per 0.23 d, resulting in a slightly "choppy" appearance at late times that is not related to the time sampling in the simulation.]

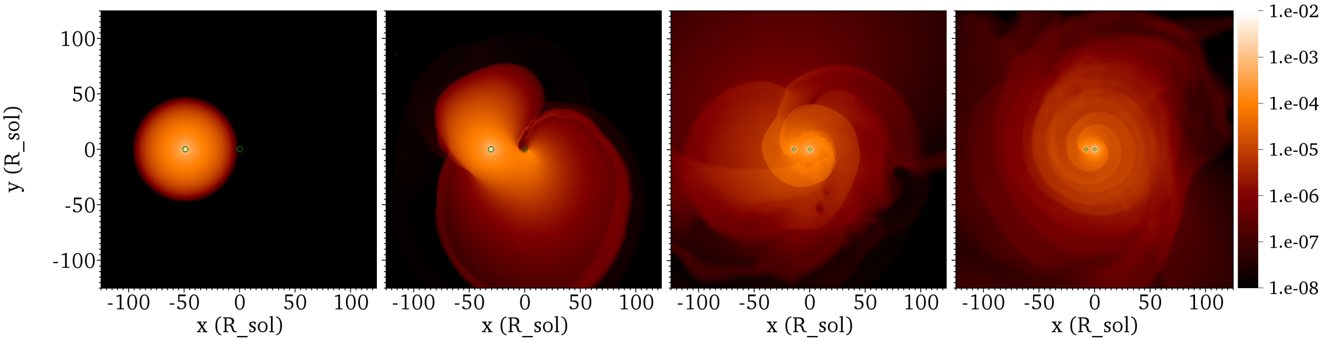

Figure 1. Density, in $\mathrm{g\,cm^{-3}}$ in a slice through the secondary and orthogonal to the xy orbital plane, for Model A (no sub-grid accretion model). The secondary is positioned at the centre with the frame rotated so that the primary particle is always situated to its left (the frame of reference is rotating with the instantaneous angular velocity of the particles' orbit). Both particles are denoted with a green circle with radius equal to the spline softening length. Snapshots from left to right are at $t = 0$, 10, 20 and 40 d.

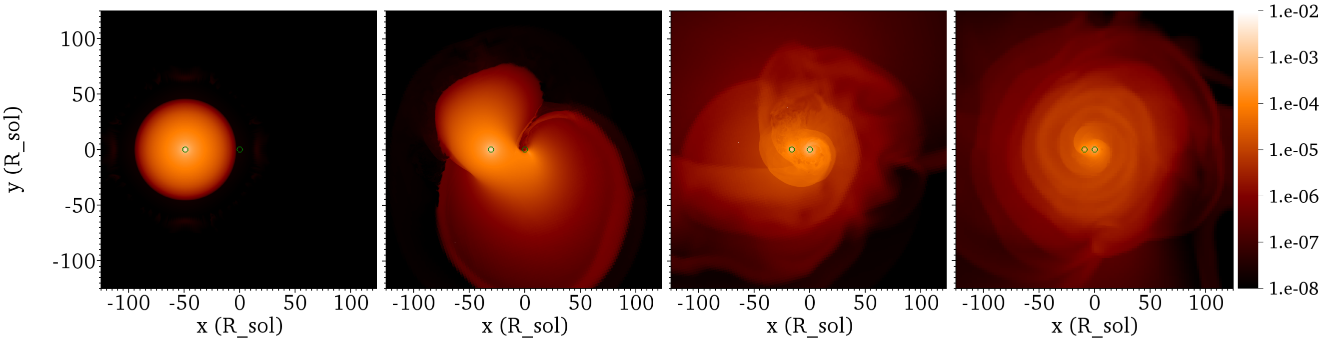

Figure 2. As Fig. 1 but now for Model B, with the Krumholz et al. (2004) sub-grid accretion model turned on for the secondary.

and $t \approx 13.5$ d, depending on the control radius. During this time $M_{\mathrm{in},2}$ increases monotonically, until it reaches a local maximum at $t \approx 15$ d, and decreases slightly before increasing again (this feature is most clearly visible in the curve for control radius $3R_\odot$, but occurs in the other curves as well). This local maximum approximately coincides with the first maximum in the inter-particle separation curve of Figure 3. As $M_{\mathrm{in},2}$ is increasing, the softening length is halved at $t = 16.7$ d. This results in a prolonged increase (modulated by small oscillations) until $t \approx 21$ d, which is the time of the third periastron, at which point the average interior mass remains roughly constant, but exhibits oscillations. These oscillations are explained by oscillations in the inter-particle separation, with local maxima of $M_{\mathrm{in},2}$ approximately coinciding with periastrons, and local minima approximately coinciding with apastrons. [Luke comments: I need to mark the locations of the periastrons and apastrons on the axes. Yisheng is working on this.] We also see a slow decline in the mean value of $M_{\mathrm{in},2}$ after $t \approx 28$ d.

The initial rise in $M_{\mathrm{in},2}$ is accompanied by a less pronounced rise in $M_{\mathrm{in},1}$ until $t \approx 13$ d (just after the first periastron), followed by a sharp decrease, in $M_{\mathrm{in},1}$. $M_{\mathrm{in},1}$ receives a 'boost' immediately following the change in softening radius at $t = 16.7$ d, as seen by the positive accretion rate even for the smallest control radius. Subsequently, $M_{\mathrm{in},1}$ experiences a gradual decay, modulated by oscillations that are approximately in phase with those of $M_{\mathrm{in},2}$.

These features can be explained as follows. As the plunging-in secondary approaches the high-density RG core, it accretes at an ever higher rate, until it has accreted a quasi-steady envelope around itself. The mean mass of this envelope over several orbits remains approximately constant. In addition, the primary retains around itself part of the remnant RG envelope. When the two particles come closer, a larger portion of the primary envelope extends into the control sphere surrounding the secondary, leading to a larger integrated mass inside the control sphere of the secondary. Likewise, this also leads to a larger integrated mass inside the control sphere of the primary particle due to the envelope around the secondary. When the particles separate, $M_{\mathrm{in},2}$ and $M_{\mathrm{in},1}$ decrease again for the same reason, and it is this back-and-forth relative motion that leads to the oscillations described above.

When the softening radius is reduced from r_s to [$Luke: r_\mathrm{s}' =$]$r_\mathrm{s}/2$, the potential well becomes twice as deep at $r = 0$ and the acceleration due to gravity of each particle gets increased everywhere within the sphere of radius r_s centred on the particle. Thus, gas flows toward the secondary until a more massive, more concentrated quasi-steady envelope becomes established. The same is true, but to a lesser extent, for the less massive primary particle. The gradual decrease in the orbital separation is mainly caused by gas dynamical friction acting on the secondary (RT08; RT12; MacLeod et al. 2017). This dynamical drag force is $\propto m_2^2$, so orbital energy will be dissipated at a higher average rate, leading to a reduction in the mean separation a. This, in turn, will result in a smaller orbital period according to Kepler's third law.

Finally, the slow decrease in the interior mass $M_{\mathrm{in},2}$ during the final ≈ 12 d for the secondary, and a similar decrease in $M_{\mathrm{in},1}$ for the primary particle, can be roughly explained by the reduction in size

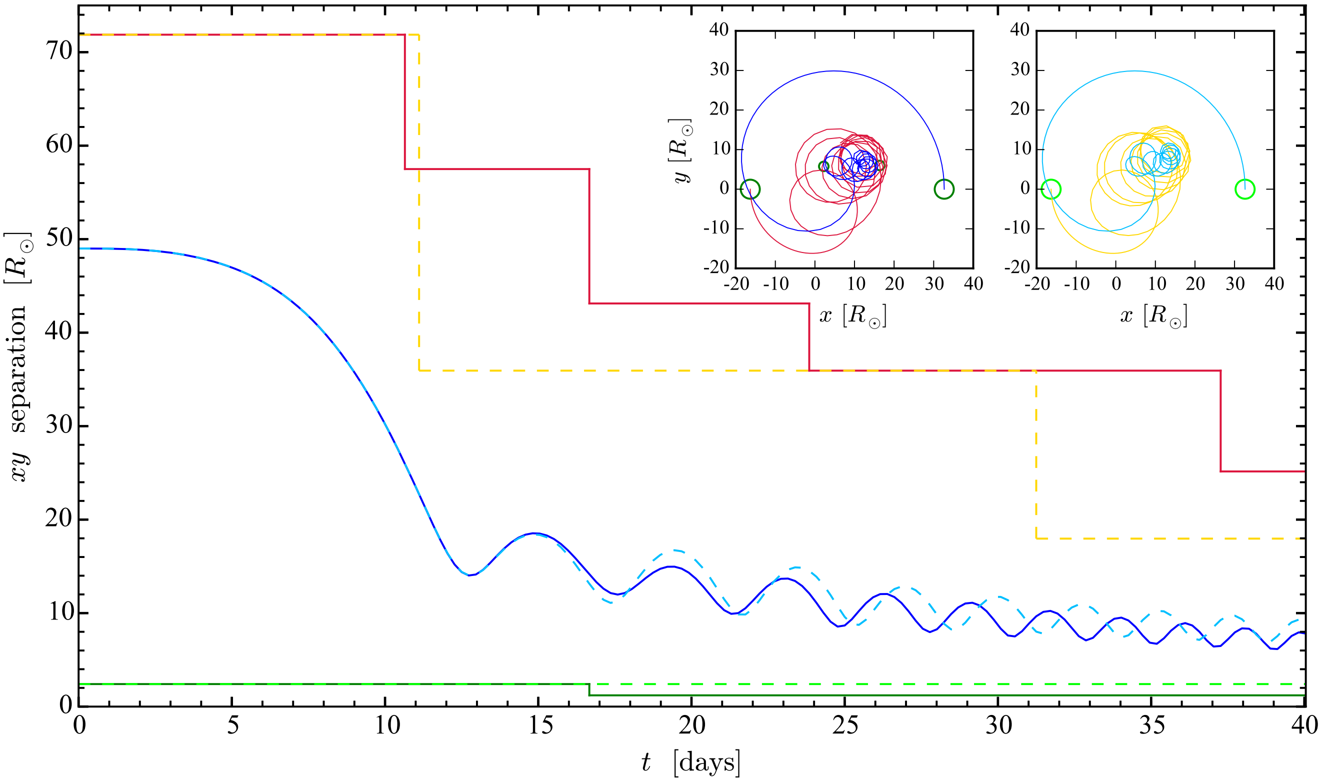

Figure 3. Inter-particle separation in the orbital plane ($z = 0$) for Model A without sub-grid accretion (solid blue) and Model B with sub-grid accretion (dashed light blue). Also shown are jagged lines denoting the radius of the spherical region of highest mesh refinement (solid red for Model A and dashed orange for Model B), and the spline softening radius (solid green for Model A and dashed light green for Model B). *Inset*: Orbit of the sink-particles, with Model A depicted on the left and Model B on the right. The centre of mass is located at the origin in each panel. The primary particle is shown in red/orange while the secondary is shown in blue/light blue. Green/light green circles with radius equal to the spline softening length are shown at $t = 0$ and, for Model A, also at $t = 16.7$ d, when the softening length is halved.

of the Roche lobes as the inter-particle separation becomes smaller. The gravitational influence of each particle extends less far out than before, so the size of the envelope that each particle can retain is reduced. [Luke comments: Can check this explanation using movies of density with Roche potential overplotted.]

3.2.2 *Accretion obtained by including a sub-grid model*

We now turn to Model B, which includes Krumholz et al. (2004) sub-grid accretion. The plots of $M_{\rm in,2}$ and $M_{\rm in,1}$ and their rates of change are qualitatively similar to those for Model A, except that we do not see pronounced oscillations. [Luke comments: Maybe not necessary to show these figures though I've included them for now for our reference. In any case, I will redo them with higher sampling rates even just for our own benefit.] Moreover, the rates $\dot{M}_{\rm in,2}$ and $\dot{M}_{\rm in,1}$ are almost always negative after $M_{\rm in,2}$ has peaked. Since the main difference between Model A and Model B is the presence of sub-grid accretion in the latter, this result suggests that the gas reservoir is primarily governed by accretion onto the secondary (though the larger softening length in Model B may also play a role).

This hypothesis is supported by [Luke: the bottom panel of] Figure 5, which shows the evolution of the [Luke: change in] secondary mass [$Luke : \Delta$]m_2, along with [Luke: the] rate of change[Luke: $\dot{m}_2$].[4] [Luke comments: Must comment on the convergence of these results with resolution.] Accretion begins at $t \approx 12$ d, coinciding with the first periastron. The accretion rate $\dot{m}_2$ peaks between $t = 16$ d and $t = 17$ d at $\dot{m}_2 \approx 2.7 M_\odot\,{\rm yr}^{-1}$. By the end of the simulation, the accretion rate is fairly steady and equal to $\dot{m}_2 \approx 0.3 M_\odot\,{\rm yr}^{-1}$, though there are significant oscillations that may be correlated with the oscillations in the inter-particle separation. [Luke comments: Should check this more carefully and mark the periastrons and apastrons on this figure too.] Thus, by the end of the simulation at $t = 40$ d the secondary has accreted $0.064 M_\odot$, for a 6.5% gain in mass, and continues to accrete steadily.

3.2.3 *Flow around the secondary*

[Luke comments: Need an intro here explaining the purpose of this section]

In Figure 6 we plot in color the local tangential velocity [Luke: $v_{\phi,2}$] with respect to the secondary in the frame of reference that rotates at the instantaneous angular velocity of the particle orbit about the secondary. Shown is a slice through the secondary orthogonal to the orbital plane at $t = 40$ d, with green circles showing the locations of the spline softening spheres. Here $v_{\phi,2}$ is normalized with respect to the Keplerian speed $v_{\rm K}$ about the secondary (corrected for the spline potential within the softening radius). A white contour delineates where $v_{\phi,2} = 0$, and the vectors show the direction and

[4] [Luke: The rate is calculated using a central difference method accurate to second order. The sampling rate is constant and approximately equal to one frame every 0.23 d.]

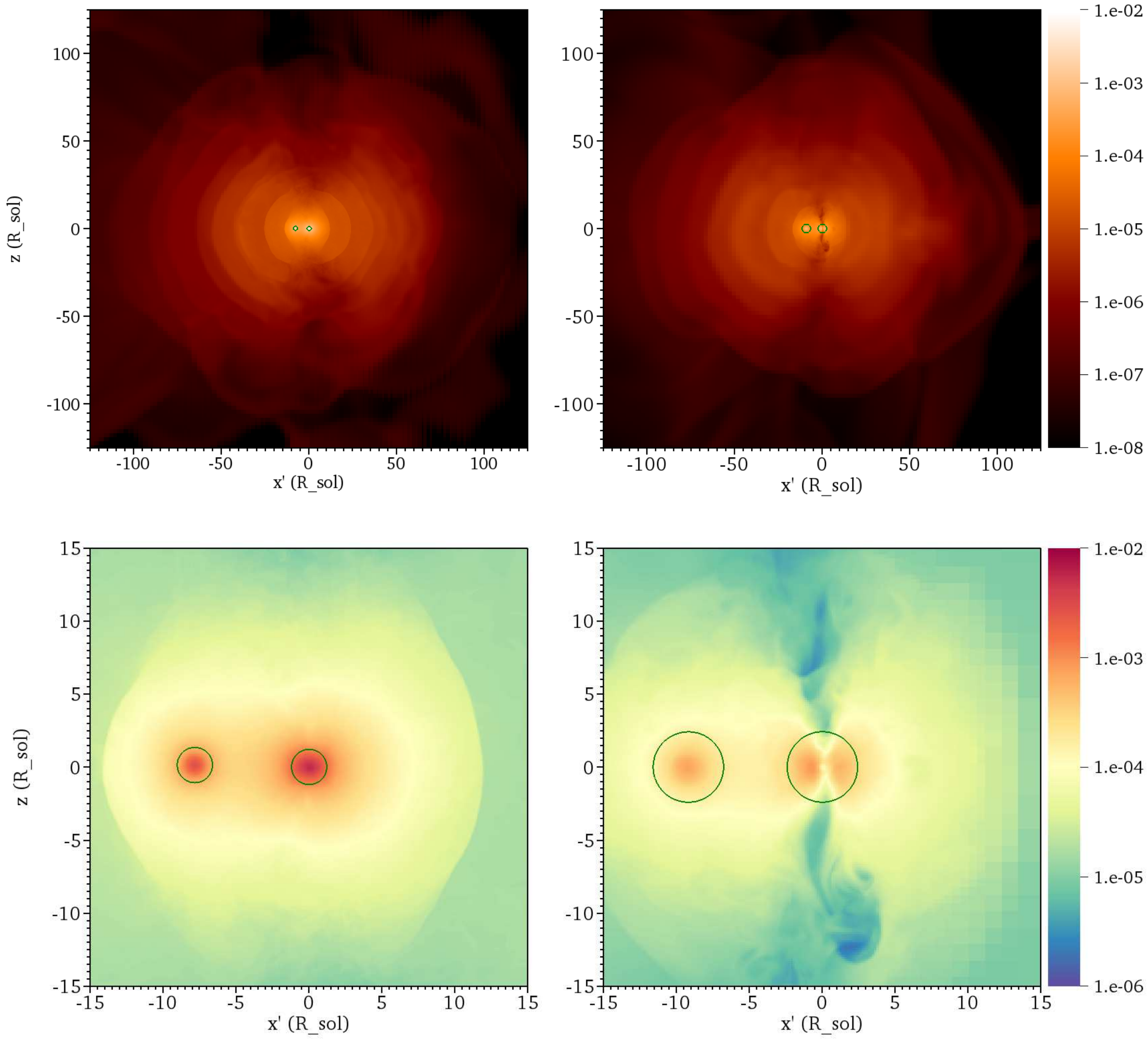

Figure 4. Gas density in $\mathrm{g\,cm^{-3}}$ viewed in a slice through both particles that is perpendicular to the orbital plane at $t = 40\,\mathrm{d}$. Model A (no sub-grid accretion) is shown in the left-hand column and Model B (Krumholz et al. 2004 sub-grid accretion) is shown in the right-hand column, while the top and bottom row show two different levels of zoom. The secondary is situated in the centre of each panel and the frame is rotated so that the primary particle is located to its left. Spline softening spheres are identified by green circles. The x'-axis is defined by the line in the orbital plane that passes through both sink particles.

relative magnitude of the velocity field of the gas projected onto the slice.

It can be seen from Figure 6 that $v_{\phi,2} > 0$ only within about 3 to $4R_\odot$ of the secondary for Model A, and about 5 to $6R_\odot$ of the secondary for Model B. Outside of this region, the gas rotates clockwise ($v_{\phi,2} < 0$, which means that it lags the orbital motion of the particles. Inside the region of counter-clockwise rotation, the vectors show that the gas also has a significant radial component $v_{r,2}$ and that this component is positive in some locations and negative in others. The magnitude of the tangential component is $\sim \frac{1}{4}V_\mathrm{K}$ within about $2R_\odot$ from the softening radius in both simulations. [Luke comments: Must comment on the convergence of these results with resolution.]

4 DISCUSSION [Eric: USE SECTION TITLE THAT BETTER DESCRIBES CONTENT]

[Luke comments: Points for discussion:

- Reducing softening length seems to result in tighter orbit...
  - what are the larger implications of this, also vis-a-vis results of ORPS16?
  - could this be why the simulations “stall” before a merger can take place? [Jason: co-rotation of the gas, and thus stalling of the orbit, will not occur in a realistic star. The "stall" radius in these simulations is still inside the convective zone.]

]

[Eric: Comparing the no-accretion case with [Luke: the] Krumholz case highlights that sustained long term accretion requires a pressure valve. The Krumholz prescription takes away both mass and pressure[Luke: , allowing] material to continue to infall at the inner boundary. If we disallow this infall, the accretion flow eventu-

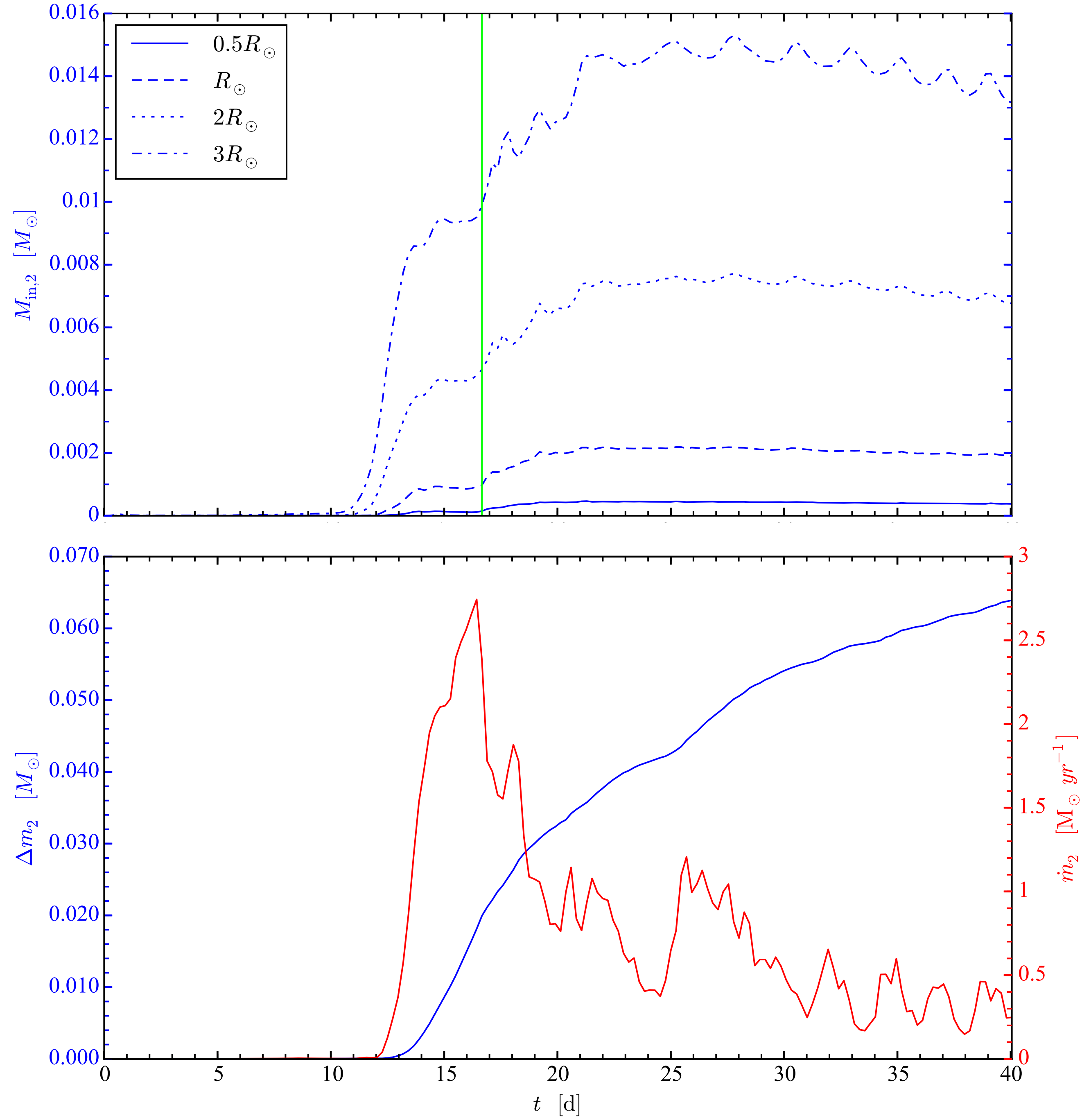

Figure 5. [Luke: **Top panel:**] 'Accretion' by the companion for Model A, which is not true accretion because no sub-grid accretion model is used. The total mass contained within spheres of various radii (see the legend) are shown in blue with labels on the left-hand vertical axis, while the rate of change of this quantity is shown in red with labels on the right-hand vertical axis. A vertical light green line marks the time at which the softening length is reduced by half. [Luke: **Bottom panel:**] Accretion by the companion for Model B, for which the Krumholz et al. (2004) sub-grid accretion model is used. The accreted mass is shown in blue (left-hand vertical axis) and the accretion rate, obtained by differentiating the accreted mass, is shown in red (right-hand vertical axis).

ally ceases. The Krumholz prescription was originally developed for protostellar accretion where material that accretes onto the central object can lose its pressure via radiation through optically thin gas. In the present case, the gas is optically thick, so we do not expect such pressure [Luke: to] release radiation. A more likely alternative is a hydrodynamic pressure release from jets. In fact, we expect that the only way to sustain accretion in these dense environments is via a jet, thereby implying a [Luke: direct] connection between jets and accretion if the latter occurs inside CE. A jet will provide a pressure release value that is finite but not as large as the Krumholz prescription. Our two cases (no accretion vs. accretion) therefore bound the two extreme cases of pressure values.]

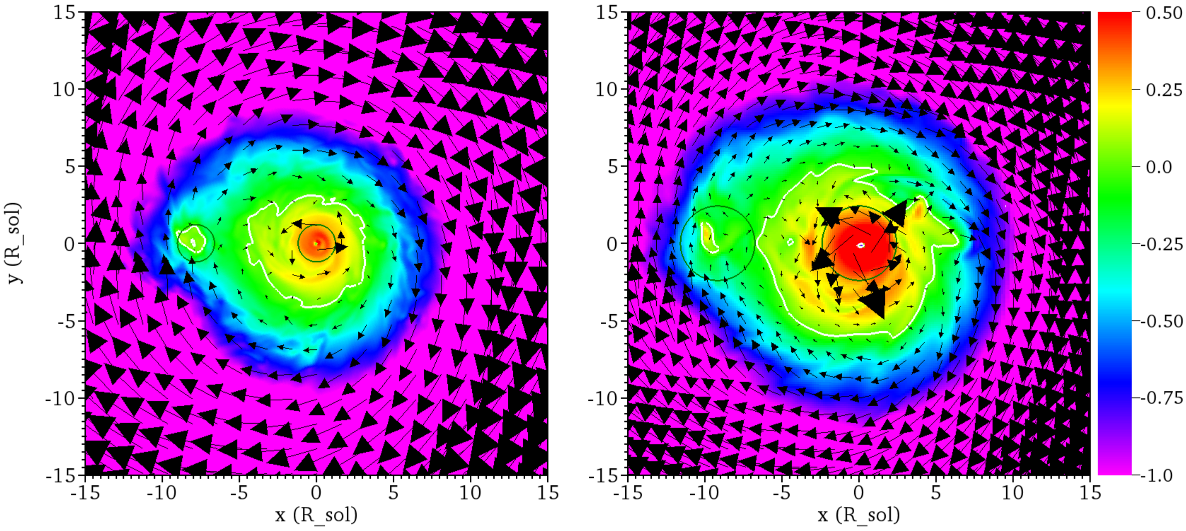

Figure 6. Slice through the orbital plane at $t = 40$ d with colour showing the tangential (with respect to the secondary, located at the centre of each panel) component of the velocity in the frame of reference rotating about the secondary with the instantaneous orbital angular velocity of the sink particles. Values are normalized by the local Keplerian circular speed around the secondary, corrected for the spline potential inside the softening sphere. The zero value, where the tangential component reverses direction, is shown by a white contour. Vectors show the direction and magnitude of the projection of this same velocity onto the orbital plane (each vector refers to the location at which its tail begins). Model A (no sub-grid accretion) is shown on the left and Model B (Krumholz sub-grid accretion) is shown on the right. Softening spheres are indicated by green circles.

[Eric: If it were the case that a jet cannot form, we would have to conclude that evidence for observed powerful outflows in PPN would not emanate from inside the CE but from the Roche Lobe overflow phase before the full CE system emerges. Interesting future work would involve studying the fate of a jet formed outside the CE as it enters the CE.]

5 CONCLUSIONS

References

Bondi H., 1952, MNRAS, 112, 195
Bondi H., Hoyle F., 1944, MNRAS, 104, 273
Carroll-Nellenback J. J., Shroyer B., Frank A., Ding C., 2013, Journal of Computational Physics, 236, 461
Cunningham A. J., Frank A., Varnière P., Mitran S., Jones T. W., 2009, ApJS, 182, 519
Edgar R., 2004, New Astron. Rev., 48, 843
Hoyle F., Lyttleton R. A., 1939, Proceedings of the Cambridge Philosophical Society, 35, 405
Iaconi R., De Marco O., Passy J.-C., Staff J., 2017, preprint, (arXiv:1706.09786)
Krumholz M. R., McKee C. F., Klein R. I., 2004, ApJ, 611, 399
Li S., Frank A., Blackman E. G., 2014, MNRAS, 444, 2884
MacLeod M., Ramirez-Ruiz E., 2015, ApJ, 803, 41
MacLeod M., Antoni A., Murguia-Berthier A., Macias P., Ramirez-Ruiz E., 2017, ApJ, 838, 56
Ohlmann S. T., Röpke F. K., Pakmor R., Springel V., 2016, ApJ, 816, L9
Ohlmann S. T., Röpke F. K., Pakmor R., Springel V., 2017, A&A, 599, A5
Paxton B., Bildsten L., Dotter A., Herwig F., Lesaffre P., Timmes F., 2011, ApJS, 192, 3
Paxton B., et al., 2013, ApJS, 208, 4
Paxton B., et al., 2015, ApJS, 220, 15
Ricker P. M., Taam R. E., 2008, ApJ, 672, L41
Ricker P. M., Taam R. E., 2012, ApJ, 746, 74
Springel V., 2010, MNRAS, 401, 791